Diffusion Analysis of NAnoscopic Ensembles: A Tracking-Free Diffusivity Analysis for NAnoscopic Ensembles in Biological Samples and Nanotechnology

*Alexander Wolf, Pierre Volz-Rakebrand, Jens Balke, and Ulrike Alexiev**

The rapid development of microscopic techniques over the past decades enables the establishment of single molecule fluorescence imaging as a powerful tool in biological and biomedical sciences. Single molecule fluorescence imaging allows to study the chemical, physicochemical, and biological properties of target molecules or particles by tracking their molecular position in the biological environment and determining their dynamic behavior. However, the precise determination of particle distribution and diffusivities is often challenging due to high molecule/particle densities, fast diffusion, and photobleaching/blinking of the fluorophore. A novel, accurate, and fast statistical analysis tool, Diffusion Analysis of NAnoscopic Ensembles (DANAE), that solves all these obstacles is introduced. DANAE requires no approximations or any a priori input regarding unknown system-inherent parameters, such as background distributions; a requirement that is vitally important when studying the behavior of molecules/particles in living cells. The superiority of DANAE with various data from simulations is demonstrated. As experimental applications of DANAE, membrane receptor diffusion in its natural membrane environment, and cargo mobility/distribution within nanostructured lipid nanoparticles are presented. Finally, the method is extended to two-color channel fluorescence microscopy.

1. Introduction

Modern microscopic fluorescence techniques in combination with single particle tracking (SPT) have proven as an indispensable tool to study the diffusive behavior of single molecules and particles in living systems.[1] They allow for direct visualization and mechanistic insight into biomolecular function without the need of measurement synchronization. Examples are the dynamic processes within the cytoplasm and in the plasma membrane of living cells,[2] virus entry and transport during infection,[3] or nanoparticle cellular uptake.[4] In particular, the tracking of individual nanoparticles has provided valuable insight into their behavior in living cells and tissues,[5] in hydrogels,[6] or within tumors.[7]

Image-based methods have the advantage of tracking many particles at the same time, allowing for parallelization.[8] But they face the principal challenges of low signal-to-noise ratio, high particle densities, motional heterogeneity, particle disappearance through fluorophore bleaching and blinking, and non-ergodic behavior of the system when extracting trajectories from the movie datasets (**Figure 1**a).[9] Advanced tracking algorithms[9,10] or a combination of super-resolution techniques such as photoactivated localization microscopy (PALM) with SPT using photoactivatable dyes[11] were introduced to account for these challenges. But still, accurate analysis of diffusion behavior remains challenging. Two main factors were identified to affect the reconstruction of tracks by particle position linking: Particle density and type of motion.[9]

Here, we introduce a tracking-free diffusion analysis method for obtaining diffusivities from single molecule/particle images that can be applied to samples of potentially unlimited density, mobility, and heterogeneity. This fully statistical technique, in contrast to previous particle image correlation spectroscopies,[12] is based on the indiscriminate calculation of distances between particle pairs, a method we call DANAE (Diffusion Analysis of NAnoscopic Ensembles). We show that omitting the laborious task of “connecting the dots”[13] to determine diffusivities, not only speeds up data analysis in DANAE but at the same time eliminates all systematic errors that might originate from trace length, background distribution, photophysical processes, or too high particle densities.

2. Results and Discussion

2.1. Concept of Diffusion Analysis of NAnoscopic Ensembles

To analyze molecule/particle diffusion in the usual way, particle localization is followed by particle tracking to characterize

---

A. Wolf, P. Volz-Rakebrand, J. Balke, U. Alexiev
Department of Physics
Freie Universität Berlin
Arnimallee 14, 14195 Berlin, Germany
E-mail: ulrike.alexiev@fu-berlin.de

The ORCID identification number(s) for the author(s) of this article can be found under https://doi.org/10.1002/smll.202206722.

DOI: 10.1002/smll.202206722

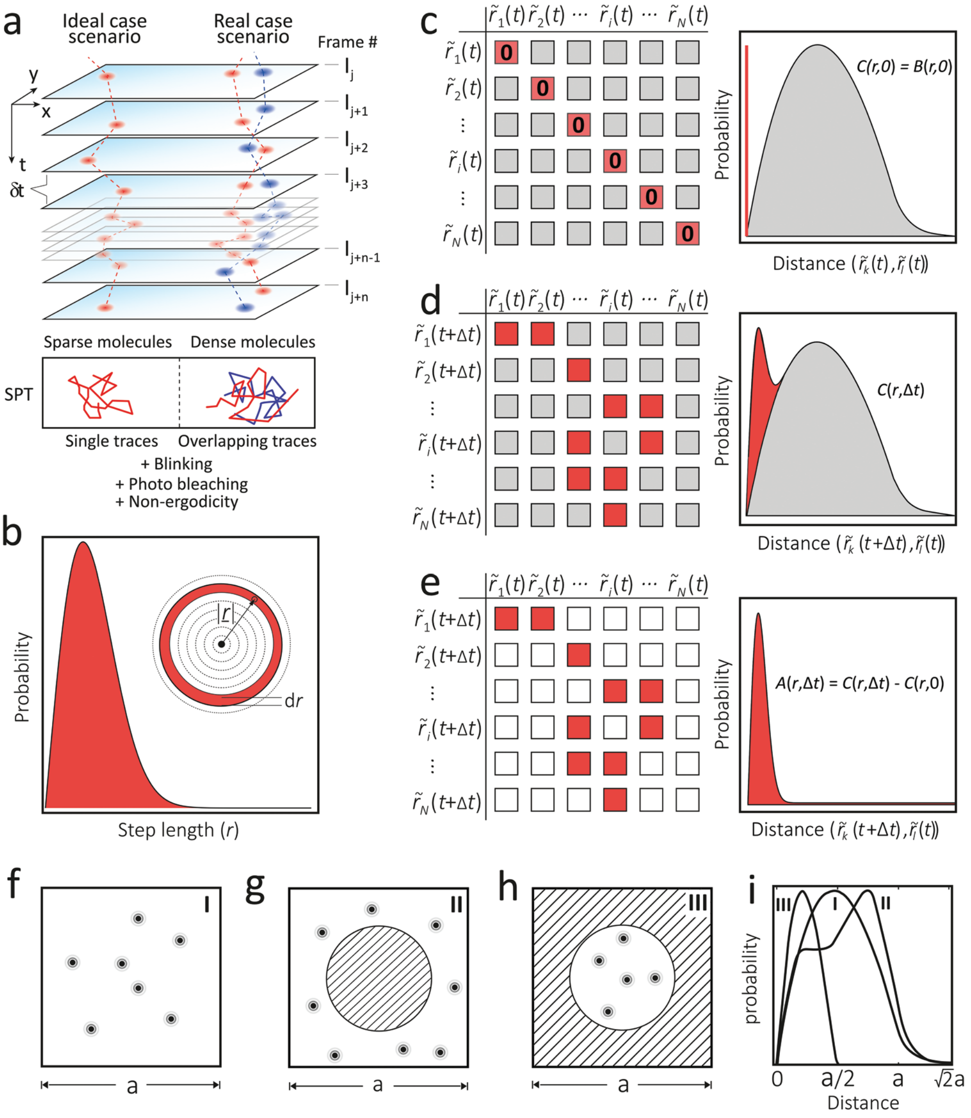

Figure 1. Concept of DANAE. a) Scheme of SPT showing an image dataset with frames *Ij* and the frame interval time Δ*t*. The image analysis method can be divided into two steps: i) particle localization (blue and red dots), and ii) particle linking (indicated by the dashed lines connecting the dots). Potential challenges for the latter are indicated. b) The step length distribution (SLD) is the probability distribution to find a particle on a radial segment *dr* in the distance $|\underline{r}|$ of its starting position after a lag time Δ*t*. c–e) Distribution functions and matrices of pairwise distances for $\Delta t = 0$, $\Delta t > 0$ and the difference distribution (SLD in red, background in grey). f–h) Different distributions in the field of view (FOV), case I–III. i) DANAE background distributions for cases I–III.

probe mobility from the tracks (for a review see, e.g., Rose et al.[8]). A semi-statistical approach to calculate diffusivities is the jump distance analysis,[14] where a step length distribution (SLD) is generated from all distances, that is, step lengths, in the extracted trajectories (Methods S1, Supporting Information). From the SLD (Figure 1b) the respective microscopic diffusion coefficient *D* can be obtained. Unlike in SPT, where only a subset of distances is determined by particle linking that may contain incorrect assignments of particle identity and consequently incorrect distances, DANAE does not establish a particle identity register. Rather, DANAE calculates all distances $|\underline{r}| = r$ between all particle pairs with indices *k, l* for all frames I_j with the frame lag (frame index) *q*

$$\left(r_{k,l}^{j}\right)_q = \left|\underline{\tilde{r}}_{k,j} - \underline{\tilde{r}}_{l,j+q}\right| \tag{1}$$

For each frame lag a histogram is generated, which corresponds to an absolute frequency distribution $C_q(r) \triangleq C(r,\Delta t)$ (Figure 1d). Since all possible distances are used, the distribution consists of distances belonging to moving particles, that is, the SLD *A*(*r*, Δ*t*), and a background distribution of all other distances *B*(*r*, Δ*t*). Thus, when the background distribution is known (grey in Figure 1c,d), the SLD (red in Figure 1d,e) can be easily determined. Fitting the background, however, introduces inaccuracies, for example, due to approximations.[12] In order to understand the differences between background estimation[12] and a statistical correct background subtraction as used here in DANAE, we briefly derive the cumulative background distribution used for approximation. Let us consider the ideal situation of a uniform random distribution of molecules *m* that can be described by a Poisson distribution with a mean of $\overline{\mu} = c\pi r^2$ and

c being the concentration of molecules or particles, which can be estimated by

$$c(m) = \frac{(\langle m \rangle - 1)}{A} \tag{2}$$

The description of the background by the Poisson distribution is valid as long as an infinitely large area A is assumed. The normalized cumulative correlation function $c_{\text{cum}}(r, \Delta t)$ is calculated as

$$c_{\text{cum}}(r, \Delta t) = f_1\, p_{\text{cum}}(r, \Delta t) + f_2\, b_{\text{cum}}(r, \Delta t) \tag{3}$$

with $f_1 + f_2 = 1$. p_{cum} is the normalized cumulative probability to find a diffusion step with a size smaller than r. The corresponding prefactor f_1 is

$$f_1 = \frac{\langle m \rangle - 1}{(\langle m \rangle - 1)\langle m \rangle} = \frac{1}{\langle m \rangle} \tag{4}$$

b_{cum} is the cumulative background function obtained from the Poisson distribution for an infinitely large area. b_{cum} equals $\frac{1}{A}\pi r^2$ and is here normalized to the area A that is occupied by one particle or molecule. The corresponding prefactor f_2 is

$$f_2 = \frac{(\langle m \rangle - 1)\langle m \rangle - (\langle m \rangle - 1)}{(\langle m \rangle - 1)\langle m \rangle} = \frac{\langle m \rangle - 1}{\langle m \rangle} \tag{5}$$

Inserting Equations (4) and (5) into Equation (3) yields

$$c_{\text{cum}}(r, \Delta t) = \frac{1}{\langle m \rangle}\, p_{\text{cum}}(r, \Delta t) + \frac{(\langle m \rangle - 1)}{\langle m \rangle} \frac{1}{A} \pi r^2 \tag{6}$$

Inserting Equation (2) into Equation (6) yields

$$c_{\text{cum}}(r, \Delta t) = \frac{1}{\langle m \rangle}\, p_{\text{cum}}(r, \Delta t) + \frac{1}{\langle m \rangle} c\, \pi r^2 \tag{7}$$

For large particle densities Equation (2) can be approximated by $c = \langle m \rangle / A$. However, when substituting this into Equation (7) the prefactor f_2 becomes 1. Consequently, the higher the particle density the larger is the fraction of c_{cum} that describes the background, thus leaving only a small fraction belonging to the diffusive part of the correlation function. Moreover, the assumption of an infinite field of view (FOV) to derive $f_2 b_{\text{cum}} = c\pi r^2$ results in a background function that is only valid for small distance values. Therefore, the outlined approximation process for background subtraction introduces large uncertainties, in particular when considering large diffusivities, as well as bleaching and blinking.

Thus, to avoid all these sources of errors and to improve the accuracy of the obtained diffusivity value, we introduce the unique feature of DANAE: our analysis tool directly gains both the shape and the size of the background distribution from the positional data. Figure 1c,d summarizes the DANAE algorithm. Since all distances of moving particles between frames vanish for the zero-lag distribution $C(r, \Delta t = 0)$, the function only contains the frequency distribution of all particle distances that are part of the background. In the corresponding matrix of pairwise distances all off-diagonal elements belong to distances of background particles (Figure 1c). Thus, the inter-particle distances in the same frame reproduce the particle distribution in the sample (grey elements in Figure 1c,d). The shape of the background is then recovered from $C(r, \Delta t = 0)$. Figure 1i visualizes the strong dependence of the background distribution $C(r, 0)$ on the local distribution of particles in the FOV. Deviations from homogeneous distributions (case I, Figure 1f,i) result in non-uniform (inhomogeneous) backgrounds, for example, due to particle clustering or confinement (case III, Figure 1h,i) or depletion (case II, Figure 1g,i) and directly affect $C(r, 0)$. This sensitivity highlights the importance for correct background subtraction but also provides a measure for the underlying geometric shape of the sample (e.g., subcellular morphology/confinement, or distribution of nanoparticle clustering upon interaction with the biological environment).

The size of the background is introduced in DANAE by a counting-based normalization factor $f(\Delta t)$. The normalization procedure multiplies $f(\Delta t)$ with the zero-lag distribution to adjust its amplitude to the background amplitude. Since for a given frame pair (frame j and frame $j+q$, where q is the frame lag) the number of particles in the SLD can only be the minimal number of particles (m) between the two frames, we can count how many particles are supposed to take part in the SLD with N as the maximum number of frames:

$$M_{\Delta t} = \sum_{j=1}^{N-q} \min\left(m_j, m_{j+q}\right) \tag{8}$$

This gives the correction factor for the zero-lag distribution by summing over all bins i of the histogram $C(r, \Delta t)$

$$f(\Delta t) = \frac{\left(\left(\sum_{\text{bin i}} C_i(r, \Delta t)\right) - M_{\Delta t}\right)}{\sum_{\text{bin i}} C_i(r, 0)} \tag{9}$$

Thus, we can now accurately calculate the SLD $A(r, \Delta t)$ (Figure 1e) from the absolute frequency distribution for lag times $\Delta t > 0$ (Figure 1d) by

$$A(r, \Delta t) = C(r, \Delta t) - f(\Delta t)\, C(r, 0) \tag{10}$$

2.2. Diffusion Analysis of NAnoscopic Ensembles Evaluation Using Monte Carlo Simulations

Next, we validated the performance of DANAE using synthetic image datasets derived from Monte Carlo simulations (MCS). Since both, particle density and mobility, may affect the accuracy of the analysis, the amount of particles diffusing in and out of the FOV has considerable consequences depending on the FOV size on particle mobility. To account for the angular restrictions on detectable particle movement around the edges of the FOV (**Figure 2**a), a FOV-corrected SLD $A_{\text{FOV}}(r, \Delta t)$ was derived (Methods S2, Supporting Information). The diffusion coefficient D is obtained from the SLD by

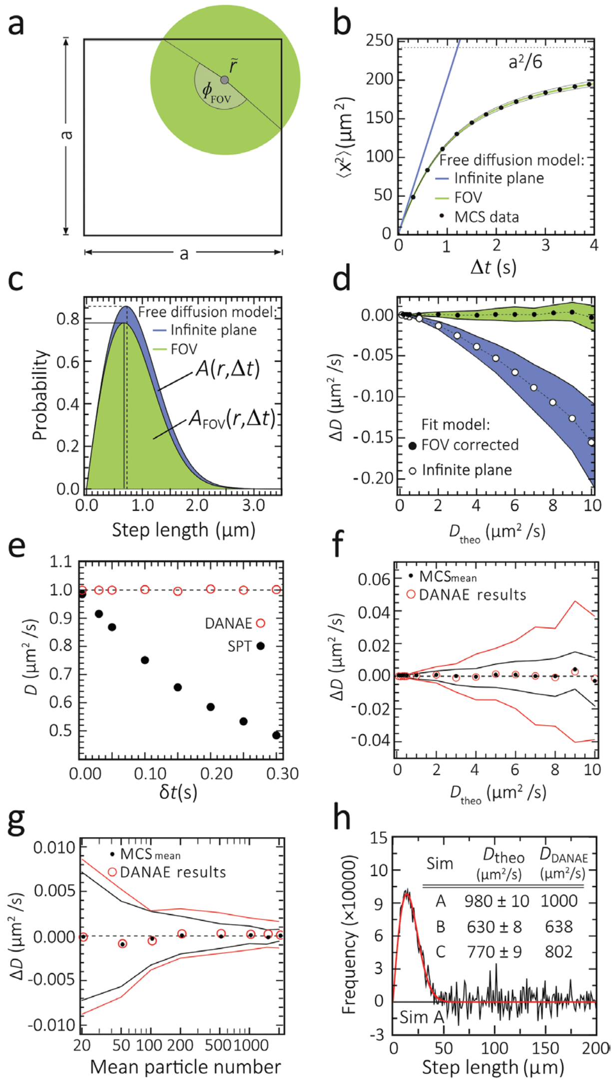

Figure 2. Boundary effects and dependence on density/diffusivity. a) Illustration of the angular restriction imposed by a rectangular FOV: step lengths falling in the radial segment indicated by the perimeter of the circle with radius r can be detected only for those particles that are localized within $\varphi_{FOV}(r)$. b) 1D simulated mean squared displacement (MSD) $\langle x^2 \rangle$ in a FOV going towards the limit at a²/6 visualized as a plot for a FOV-corrected diffusion and an infinite plane model. $D_{input} = 100\ \mu m^2\ s^{-1}$; particle number: 800. c) Difference in relative size and shape between the SLDs from the plots in (b) for the infinite plane (blue) and for the FOV-corrected model (green). d) Corresponding diffusion values given as the deviations from the input diffusivity D_{theo} for increasing values of D. e) Comparison of diffusivities obtained from DANAE and from SPT generated SLDs as a function of the frame interval time δt for a dense sample with one population. f) Dependence of DANAE accuracy on particle mobility. The MCS generated input values varied between 0.1 and 10 μm² s⁻¹. g) Dependence of DANAE accuracy (given as deviations from the input diffusivity $D = 1\ \mu m^2\ s^{-1}$) on particle density and comparison to true D from simulation. The mean particle numbers per frame: 20–2000. h) Comparison of DANAE-generated SLDs and determined diffusivities to input diffusivities for three cases of ultrafast particle diffusion (errors denote intrinsic standard deviation from Brownian motion). Shown is the SLD and FOV-corrected fit from simulation A with $D = 980\ \mu m^2\ s^{-1}$ and most step lengths exceeding the mean particle distance $z \approx 4\ \mu m$ by more than 300%. Particle number: 2500; $\delta t = 0.1$ s. Simulations in (b)–(h) represent Brownian motion.

$$A_i\,(r, D_i, \Delta t)\,\mathrm{d}r = \frac{1}{4\,D_i\,\Delta t}\exp\left(-\frac{r^2}{4\,D_i\,\Delta t}\right)2\,r\,\mathrm{d}r \tag{11}$$

The mean squared displacement (MSD)-plots in Figure 2b for an infinite plane and for the FOV-corrected model together with the differences in the corresponding SLDs (Figure 2c) and the dependence on particle mobility (Figure 2d) clearly show that neglecting FOV-constrains underestimates the diffusion coefficient D. The faster the diffusion the larger is the error and the deviation from the input value D_{theo} (Figure 2d). Figure 2e highlights the superiority of DANAE compared to conventional SPT. Using $D_{theo} = 1\ \mu m^2\ s^{-1}$ our analysis shows that even for a frame interval time $\delta t = 30$ ms the SPT-derived SLD shifts to smaller distances leading to an underestimation of D (Figure S1, Supporting Information). For larger Δt this deviation increases while the DANAE-derived values reproduce D_{theo} (Figure 2e). The broadened shape of the SPT-derived SLD (Figure S2, Supporting Information) might be incorrectly interpreted as being the result of additional diffusing particle populations. This assumption would improve the fit even though no such additional populations exist. The same holds true for increasing particle densities (Figure S3, Supporting Information). Evaluation of large MCS datasets confirms that DANAE reliably produces accurate diffusivities with $\Delta D < 0.02\%$ and the mean values lie within the simulations spread (Figure 2f,g). The results are even improved when using higher particle numbers due to better statistics (Figure 2g), a result not possible with SPT[9] (Figure S4, Table S1, Supporting Information). Figure 2h and Figure S3, Supporting Information, show an extreme example of ultrafast and ultradense diffusion. Most step lengths were multiples of the average inter-particle distance. However, DANAE provides correct diffusivities with an error <5% in a situation where no tracking/trace reconstruction-based algorithm could deliver meaningful results.

Besides particle density and rapid diffusion, also fluorophore blinking and bleaching might introduce artefacts. In SPT, this results in mismatching of particle pairs after dis-/reappearing events (Figure S5, Supporting Information) and the depletion of the SLD amplitude for higher lag times (**Figure 3**a,b, Figure S6, Supporting Information). Consequently, the SPT-recovered D-values were underestimated (Figure 3c) and an increase in the standard deviation was observed (Figure 3d). Under the same experimental conditions of bleaching and blinking, however, the analysis results from DANAE were not affected (Figure 3c,d). Using different bleaching/blinking scenarios, the robustness of DANAE to produce the true D is demonstrated in Figure 3e,f.

2.3. Application of Diffusion Analysis of NAnoscopic Ensembles to Nanoparticle Morphology and Membrane Receptor Diffusion

Nanostructured lipid carrier (NLC) are an interesting class of nanoparticles for the delivery of cargo to tissue and cells, and are composed of physiological and biocompatible lipids, surfactants and co-surfactants (for a recent review see Chauhan et al.[15]). Importantly, NLCs provide increased stability and cargo loading compared to solid lipid nanoparticles. We previously analyzed the morphology and cargo loading of NLCs

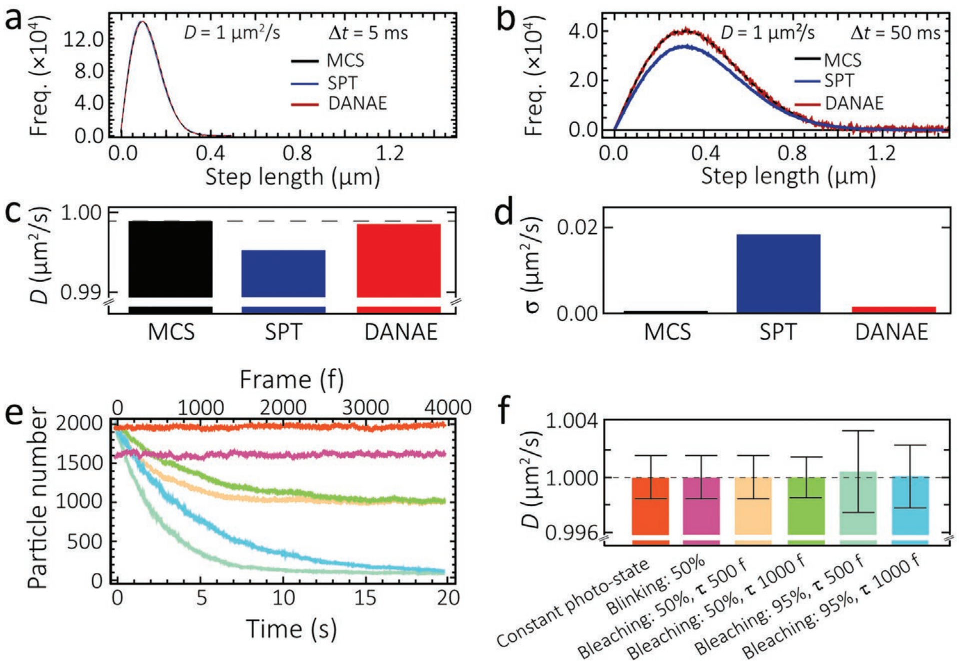

Figure 3. DANAE under experimental conditions. a–f) Photobleaching and blinking effects. Comparison of extracted SLDs from simulated datasets with 50% of 2000 particles blinking ($\tau_{\text{on}} = 50$ ms, $\tau_{\text{off}} = 25$ ms) for lag times of a) 5 ms and b) 50 ms. Shown are the SLDs from simulation (black), and from analyses with SPT (blue), and DANAE (red). The amplitude of the SPT-based SLD in (b) is significantly reduced due to failing to connect traces with holes. c) Comparison of D, and d) standard deviation σ_D from the fit of a SLD for 10 lag times (q running from 1 to 10 in Equation (1) for DANAE and SPT. The simulation input values (MCS) are given. e) Particle numbers over frames for different amplitudes (in %) and time constants (in frames) simulating blinking and bleaching. f) Corresponding diffusivity analysis with DANAE after 50 iterations of MCS based simulations.

using single molecule total internal reflection fluorescence microscopy (smTIRFM).[5a] **Figure 4** highlights the potential of DANAE for analyzing the different cargo diffusivities in the NLC, thereby providing insight in both stability, cargo distribution/loading capacity, and drug release. The latter could only be observed with DANAE because of the accurate determination of the small subpopulation of moving cargo molecules with interparticle distances that correlate with the size of the NLC (Figure 4b–d). This subpopulation thus presents those cargo molecules that may diffuse out of the NLC.

To show another biomedical relevant application, we analyzed membrane receptor diffusion data with DANAE. Since G-protein coupled receptors (GPCRs) comprise the largest class of transmembrane receptors and are targets of numerous drugs, we used as an important example the class A GPCR rhodopsin that is highly concentrated in disk membranes[16] (**Figure 5**a) and thus would pose a challenge in SPT-based analyses. Moreover, differences in GPCR interactions as receptor dimers, monomers, constitutive dimers, and density dependent dimers were found recently among representative GPCRs from class A, B, and C.[17] Such dynamic receptor properties substantially affect GPCR function from activation to deactivation.[18]

Constitutive active opsin mutants are associated with eye diseases like retinitis pigmentosa and congenital night blindness.[16,19] The constitutive activity of opsin is known to be very low at neutral pH and to increase substantially at acidic pH,[20] but the effect on active receptor diffusion under these conditions was not determined so far. Therefore, we applied DANAE to determine the diffusivities of active opsin and compared DANAE with SPT-based analyses.

smTIRFM of opsin diffusion as a function of pH was performed as described recently, using affinity labeling of the active receptor by a fluorescent G-protein-derived peptide ($\text{pG}_\text{T}\alpha$-F).[16,21] DANAE reveals opsin diffusion at pH 6 as free diffusion with $D_{\text{inactive}} = 2.85 \pm 0.05$ µm² s^{-1}, while the SPT-derived value D_{inactive} (SPT) = 1.09 ± 0.05 µm² s^{-1} underestimated the diffusivity (Figure 5b,e), in agreement with our predictions from DANAE evaluations using MCS. At pH 3 (Figure 5c), we observed confined diffusion of the active receptor with a confinement length of $L_{\text{active}} = 157 \pm 4$ nm and $D_{\text{active}} = 0.08 \pm 0.01$ µm² s^{-1} (Figure 5f) according to Equation (14). Using SPT, the respective MSD-plot lacks confinement (Figure 5f), again showing the sensitivity of diffusion analysis results to the drawbacks in the respective analysis tools. Interestingly, confinement and $D \approx 0.1$ µm² s^{-1} was detected earlier for light-activated rhodopsin at low particle densities.[21] Thus, our DANAE results indicate a common diffusion behavior of the active visual receptors under various conditions and suggest similar interactions with signaling molecules,[22] also in the case of constitutive activity. Such information is highly useful in the quest for the appropriate treatment of the disease.

In living systems, such as the eyes, non-ergodic behavior and aging have been observed and might be intimately connected to biological function.[2b,23] As DANAE and other SLD-based methods do not employ averaging, ergodic properties are not directly obvious. However, non-stationary behavior can be analyzed and should result in time-dependent amplitudes for the individual diffusion components, as tested in Figure 5g. The analysis of the active GPCR opsin diffusion shows no

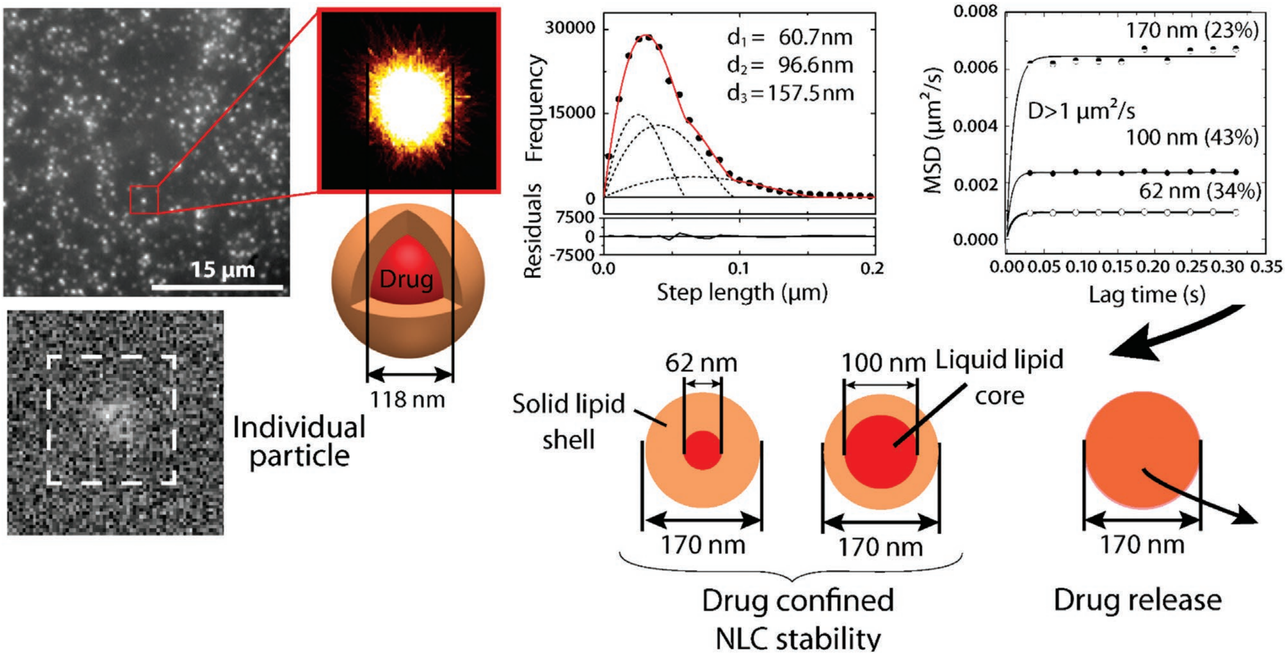

Figure 4. DANAE analysis of cargo diffusion in NLCs. a) smTIRFM microscopy images as published in Boreham et al.[5a] b) DANAE analysis of the diffusivity of the amphiphilic dye (model drug) loaded to the NLC.[5a] The SLD shows confined diffusive behavior with three confinement lengths, in contrast to the SPT analysis shown in (a). c) The MSD plot shows the respective diffusivities and confinement length; the relative fractions are indicated. DANAE not only reveals the two different sizes of the drug-filled liquid core shown as dark red circles in (d) as published in ref. [5a] but identifies the fraction of cargo molecules (23% and shown in dark orange) that may diffuse out the NLC based on the distribution within the whole NLC.

time-dependent amplitude changes (Figure 5d), as expected for active receptor binding/unbinding events in equilibrium. Thus, our DANAE method could be useful in the evaluation of dynamic GPCR dimer formation as the oligomeric status of class A and B GPCRs is still hotly debated and remains to be fully explored.[17]

2.4. Two-Color Channel Microscopy with Diffusion Analysis of NAnoscopic Ensembles

Finally, we introduce the application of DANAE to two-color microscopy experiments (2cDANAE) as a natural extension of DANAE from calculating time-separated distances within one file to calculating distances within two files in 2cDANAE. The two files represent two spectral detection windows of the same sample with two different fluorophores. This is especially useful when studying the interaction of particles during the observation time, for example, the formation of GPCR oligomers as outlined above. While colocalization is a useful tool for analyzing individual images, co-diffusion analysis is complicated by the discrimination of random cross-over of particles, that is, uncorrelated movement, from correlated motion, that is, co-diffusion of interacting molecules. This challenge is similar to the problem already solved with (one color) DANAE where the moving particles are self-correlated, while in 2cDANAE the moving particles are cross-correlated between the two files. An example of the analysis of two synthetic data sets with uncorrelated and correlated motion is shown in Figure S7, Supporting Information. After the analysis by 2cDANAE a SLD of zero was obtained for uncorrelated diffusion (Figure S7a,c, Supporting Information), while for the correlated mobility of the particles indeed the SLD of the co-diffusing particles are obtained (Figure S7b,c, Supporting Information). The 2cDANAE method represents a robust and simple alternative to the recently introduced method of single pair fluorescence resonance energy transfer measurements of GPCRs in livings cells[17] and could be used to analyze the dynamics of the various flavors of GPCR oligomers in the future.

3. Conclusion

In essence, DANAE and 2cDANAE provides an assumption-free and fast approach for the diffusivity analysis from single particle microscopy data and we expect that this method expands the scope of single-molecule imaging for life-cell and in vitro microscopy towards ultrahigh densities/diffusivities. Omitting the reduction of particle datasets to traces, which per se eliminates the laborious task of "connecting the dots,"[13] in particular eliminates all systematic errors resulting from predetermined parameters (connection criterion, trace length, background), photochemical processes, and diffusion/density induced particle mismatching. Thus, DANAE is very well suited to accurately discriminate populations with different mobility or diffusive modes, including the real diffusivity of oligomeric molecules or particle clusters by 2cDANAE. As DANAE is not affected by blinking and bleaching, it also may be applied to defocusing effects when diffusion occurs in 3D. Out of focus particles can be viewed similarly to blinking particles. In the

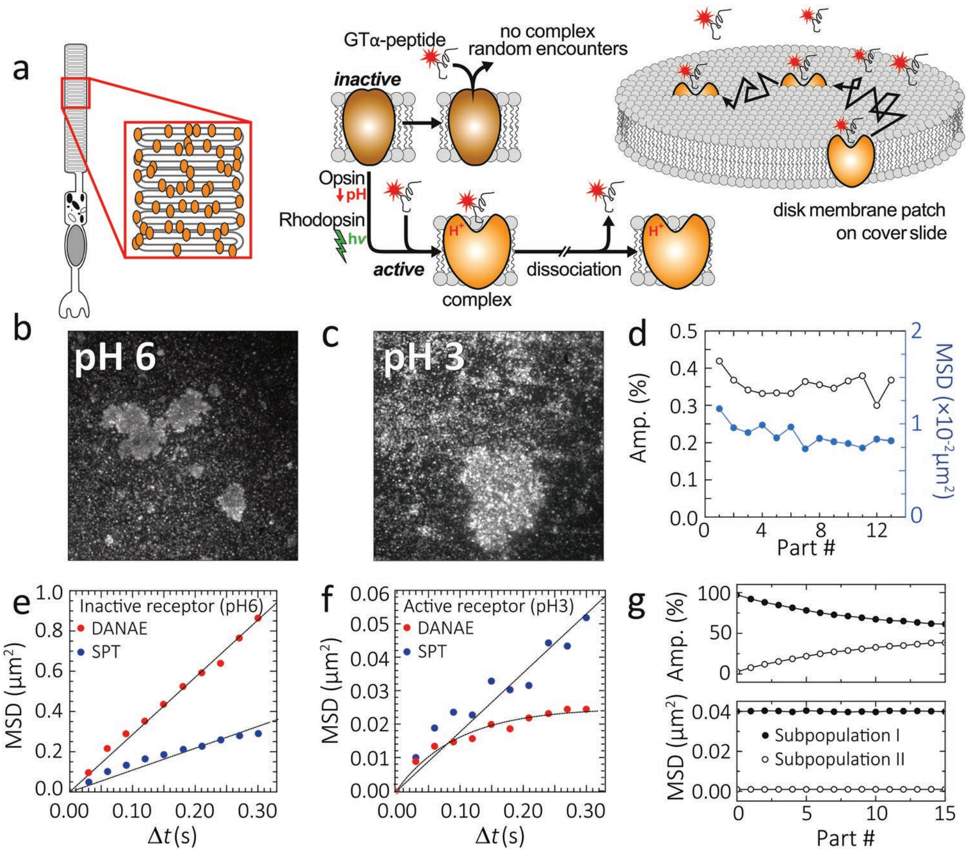

Figure 5. Diffusion analysis of ligands to the membrane receptor opsin. a) GPCR Rhodopsin is densely packed in stacks of disk membranes in rods of the mammalian eye. At low pH, its apoprotein opsin configures into an active-like state allowing for the transient binding of fluorescently labelled G-protein binding domain pGTα-F. Opsin diffusion in the disk membrane can thereby be measured with fluorescence microscopy. b) TIRFM maximum intensity projection at pH 6 and c) pH 3 of pGTα-F. The rod outer segment disk membrane fragment in (c) is clearly visible due to an increased presence of pGtTα-F at the active receptor at pH 3. d) Relative amplitude and MSD values extracted by DANAE for the active receptor as a function of movie parts with 2000 frames. MSD plots for e) the inactive and f) the active opsin receptor. Mobile fractions extracted by DANAE (red) and SPT (black) are compared. g) Simulation of increased trapping events during the observation time resulting in two sub-populations, a mobile and an immobile. DANAE correctly analyzes MSDs that are constant over time and relative amplitudes that are changing.

future, this fully-statistical DANAE method can be combined with advanced particle localization methods to further improve analysis speed and accuracy,[9,24] with Hidden-Markov modeling methods for diffusivity transition analysis,[25] with 3D particle position reconstruction methods,[26] or with artificial intelligence tools to reconstruct the tracks of different populations from their diffusivities.

4. Experimental Section

Monte Carlo Simulations: Generation of synthetic image datasets: Validation of DANAE was performed on synthetic image data sets. These data sets were generated by Monte-Carlo simulations (MCS). MCS was performed with a self-written script in Python3 with m_{bath} particles in a quadratic 2D box with side length a_{bath}. Movement of the particles followed a free diffusion random walk model with each step being the result of a pseudo random number generated from a Gaussian probability density function with $\mu = 0$ and $\sigma^2 = 2\ D\ \delta t$ with periodic boundary conditions at the sides of the box representing the bath. Positional data were extracted in a quadratic FOV at the center of the box with side length a_{fov} thus limiting the number of extracted particles to be around

$$\langle m_{\text{fov}} \rangle = m_{\text{bath}} \left(a_{\text{fov}} / a_{\text{bath}} \right)^2 \tag{12}$$

and exported with 16 digit accuracy without saving particle identity. If not stated otherwise, all simulations were performed with a pixel (px) size of 74×74 nm^2, $a_{\text{fov}} = 512 \times 512$ px, and a frame interval of $\delta t = 5$ ms for 4000 frames in total.

Two sets of simulations were performed to evaluate the accuracy of DANAE, one varying D itself and one varying $\langle m_{\text{fov}} \rangle$. In the first set input diffusion constants varied between 0.1 and 10 µm^2 s^{-1}. For each diffusion constant 50 simulations were performed with $\langle m_{\text{fov}} \rangle = 500$ and exported while also calculating and saving the actual MSD from the simulation data before particle identity is erased ($a_{\text{bath}} = 4048 \times 4048$ px). In the second set of simulations mean particle densities were varied between 80 and 2000 particles in the FOV while keeping $D = 1$ µm^2 s^{-1}. Again 50 simulations were performed for each particle density and the actual MSDs were exported ($a_{\text{bath}} = 1024 \times 1024$ px).

Single Particle Tracking Analysis: For the SPT analyses of the data, a self-written script in Python3 was used. The algorithm finds nearest neighbors between consecutive frames by assigning each particle an index and calculating all inter-particle distances and sorting them from the smallest to the longest distance up to a cutoff distance. Assignment of particles to nearest neighbors was then performed in a bijective manner. The indices of consecutive nearest neighbors are sorted into lists representing traces (e.g., {Particle 24 in frame 7, Particle 43 in frame 8, Particle 17 in frame 9 ...}). From these traces jump distance histograms (SLDs) were generated by calculating the distances between the connected particles for a given t_{lag} (lag time).

Simulations of Statistical Effects on Single-Particle Microscopy Experiments: Simulation of blinking/bleaching: Before exporting the particle positions from the MCS a population of particles $\{m_{\mathrm{ISC}}\}$ was subjected to temporary deletions (simulated blinking). Two characteristic blinking times, τ_{on} and τ_{off}, were set for each simulation and individual on- and off-times of particles were generated from exponential probability density functions. 50 simulations were performed with $\langle m_{\mathrm{fov}} \rangle = 2000$ and $D = 1\ \mu\mathrm{m}^2\ \mathrm{s}^{-1}$. Bleaching simulations were conducted similar to blinking, but without particles returning to the on-state. Two different bleaching populations $\{m_{\mathrm{destr}}\}$ were selected representing 50% and 95% bleached (i.e., destroyed) particles out of 2000 particles. The characteristic off-times were 50% and 75%, respectively, of the overall simulation time of 4000 frames and 50 simulations were performed for each scenario.

The simulation of trapping-based non-stationary effects was essentially the same as for bleaching, however particles were not destroyed but forced to move around the trapping position in a small Gaussian shaped probability volume that mimics the localization accuracy in microscopy experiments. For the simulations of blinking, bleaching and trapping a_{bath} was 4048×4048 px.

The authors are indebted to Prof. Helmut Grubmüller from the Max Planck Institute for Biophysical Chemistry in Göttingen, Germany, for challenging their algorithm through the simulations in Figure 2h, which were produced in a similar fashion as the MCS and sent to them. The parameters for these simulations were: $a_{\mathrm{bath}} = 400\ \mu\mathrm{m}$, $a_{\mathrm{fov}} = 200\ \mu\mathrm{m}$, $m_{\mathrm{bath}} = 10\,000$, $\delta t = 100$ ms. The total number of exported frames was 1000.

Furthermore, synthetic data sets were generated using MSC to compare the performance of DANAE to results presented by Chenouard et al.[9] Simulations were performed with the following parameters: $a_{\mathrm{bath}} = 1024\ \mu\mathrm{m}$, $a_{\mathrm{fov}} = 512\ \mu\mathrm{m}$, $m_{\mathrm{bath}} = 20\,000$, $\delta t = 1$ s. The total number of exported frames was 100. 100% of particles underwent blinking with $\tau_{\mathrm{on}} = 20$ s and $\tau_{\mathrm{off}} = 80$ s (Figure S4, Table S1, Supporting Information).

Sample Preparation: Peptide synthesis of the synthetic peptide mimicking the C-terminal segment of the transducing α-subunit, (VLEDLKCVGLF, $\mathrm{pG_T}\alpha$) was performed at the Institute of Biochemistry, Universitätsmedizin-Charite Berlin, and afterwards fluorescently labeled with Atto-647N-maleimide (Atto-Tec, Germany), yielding $\mathrm{pG_T}\alpha$-F.[21]

Bovine retinae were purchased from J. A. Lawson Corp (Lincoln, NE). Rod outer segment (ROS) membranes were extracted from retinae at low ionic strength[27] (buffer: 15 mm $\mathrm{NaH_2PO_4}$, 1 mm $\mathrm{MgCl_2}$, 0.1 mm EDTA-Na) and purified by discontinuous density-gradient centrifugation. Remaining soluble and membrane-associated proteins were removed by repeated washing in low ionic strength buffer and a subsequent purification step by continuous sucrose-density centrifugation. The ROS samples were stored at −80 °C.

Opsin preparation from ROS was initiated by illumination with light of $\lambda > 435$ nm and 50 mm hydroxylamine and 2% bovine serum albumin.[28] Membranes were washed with low ionic strength buffer to remove peripheral proteins and retinaloxime. The opsin concentration was calculated using the absorption maximum at 280 nm ($\varepsilon_{280\mathrm{nm}} = 65\,000\ \mathrm{M^{-1}\ cm^{-1}}$).[29] Prior to the measurements the sample was stored in 10 mm MES pH 6.0 at −80 °C.

Single Molecule Total Internal Reflection Fluorescence Microscopy Measurements: The TIRF microscopy setup,[5b] consisted of an inverted wide-field microscope (Olympus IX-71) with a 60x oil immersion objective (PLAPON60xOTIRFM, Olympus) with a numerical aperture of 1.45. Excitation of the samples was achieved with a 21 mW 623 nm helium-neon laser (1145P/JSD Uniphase). Fluorescence emission was collected by the same objective and separated from excitation light and possible scattering by a dichroic beam splitter (Z633RDC, Chroma Technology, Inc.) and a long pass filter (HQ655LP, Chroma) in the emission path. Emission was detected by a cooled electron-multiplying charge coupled device camera (ImagEM C9100-13, Hamamatsu). Details of the setup are published.[5b] The recorded movies consist of 2000 frames with a frame rate of 31 ms/frame and a FOV of 512 × 512 pixels with a pixel length of 74 nm that was measured with proper gratings. The positions of the fluorescent spots were identified using the algorithm DAOSTORM.[30]

Sample preparation for TIRFM measurements of opsin membrane patches were done as described.[21] 36 µM opsin in disk membranes were used in 10 mm MES buffer (pH 6.0). Tracking measurements were performed with 60 nM $\mathrm{pG_t}\alpha$-F.[21] For active receptor measurements the buffer was exchanged to 50 mm citrate buffer (pH 3.0).

To analyze the SLDs of opsin diffusion and of cargo diffusion in NLCs the FOV-corrected SLD (see Supporting Information) and a probability density function describing the distribution of distances r between two random points in a circle (circular confinement) were used:[31]

$$P_i(r) = \sum_i^N A_i \left(\frac{2r}{L_i^2} - \frac{4r \sin\left(\frac{r}{2L}\right)}{\pi L_i^2} - \frac{r^2 \sqrt{4L_i^2 - r}}{\pi L_i^4} \right) \tag{13}$$

A_i are the amplitudes and L_i the confinement radii of the ith subpopulation. A prerequisite for the use of Equation (13) is the prior knowledge of confined diffusion. This can be established by fitting a general radial probability distribution[21,32] to the SLD histograms obtained at various lag times and generating the MSDs. For a 2D circular confined system, the MSD versus time plot reaches a plateau determined by the confinement size, that is, there is no lag time dependence of the MSDs for higher lag times. To obtain the confinement length d (d represents the diameter) for the subpopulations, the MSDs were fitted with the time-dependent MSD function for a circular confinement:[33]

$$\mathrm{MSD}\,(t) = L^2 \left[1 - 8 \sum_n \exp\left(-\frac{\beta_n^2 D_{t_{\mathrm{lag}}}}{L^2} \right) \frac{1}{\beta_n^2 - 1} \frac{J_0^2(\beta_n)}{J_1^2(\beta_n)} \right] \tag{14}$$

where $L = d/2$ is the confinement radius, D the diffusion coefficient and $J_n(\beta_n)$ the Bessel functions of order n from $n = 1$ to 100.

Diffusion Analysis of NAnoscopic Ensembles Script: The DANAE algorithm exists as a program in Python3 and the code is available in the Supporting Information.

Supporting Information

Supporting Information is available from the Wiley Online Library or from the author.

Acknowledgements

This work was funded by the Deutsche Forschungsgemeinschaft (DFG, German Research Foundation)—Project ID 221545957- SFB 1078, project A2 and Project ID 431232613—SFB 1449, project A04 to U.A.

Open access funding enabled and organized by Projekt DEAL.

Conflict of Interest

The authors declare no conflict of interest.

Author Contributions

U.A. conceived and supervised the project. A.W. developed the algorithm. A.W. and P.V.-R. generated, analyzed, and interpreted the simulated data. A.W., P.V.-R., and U.A. contributed to the theoretical background of the project. J.B. and U.A. analyzed and interpreted the experimental data. U.A. and A.W. wrote the manuscript. All authors discussed the results and commented on the manuscript.

Data Availability Statement

The data that support the findings of this study are available in the supplementary material of this article.

Keywords

molecular interactions, nanocarriers, nanoscopic diffusion, single molecule fluorescence, tracking-free

Received: October 31, 2022
Revised: December 16, 2022
Published online: January 20, 2023

---

[1] a) C. Manzo, J. A. Torreno-Pina, P. Massignan, G. J. Lapeyre Jr., M. Lewenstein, M. F. G. Parajo, *Phys. Rev. X* **2015**, *5*, 011021; b) A. Dupont, D. C. Lamb, *Nanoscale* **2011**, *3*, 4532.
[2] a) B. R. Parry, I. V. Surovtsev, M. T. Cabeen, C. S. O'Hem, E. R. Dufresne, C. Jacobs-Wagner, *Cell* **2014**, *156*, 183; b) A. V. Weigel, B. Simon, M. M. Tamkun, D. Krapf, *Proc. Natl. Acad. Sci. U. S. A.* **2011**, *108*, 6438; c) M. J. Saxton, K. Jacobson, *Annu. Rev. Biophys. Biomol. Struct.* **1997**, *26*, 373.
[3] B. Brandenburg, X. W. Zhuang, *Nat. Rev. Microbiol.* **2007**, *5*, 197.
[4] a) H. Jin, D. A. Heller, M. S. Strano, *Nano Lett.* **2008**, *8*, 1577; b) S. Ashraf, A. H. Said, R. Hartmann, M. A. Assmann, N. Feliu, P. Lenz, W. J. Parak, *Angew. Chem., Int. Ed.* **2020**, *59*, 5438.
[5] a) A. Boreham, P. Volz, D. Peters, C. M. Keck, U. Alexiev, *Eur. J. Pharm. Biopharm.* **2017**, *110*, 31; b) P. Volz, A. Boreham, A. Wolf, T.-Y. Kim, J. Balke, J. Frombach, S. Hadam, Z. Afraz, F. Rancan, U. Blume-Peytavi, A. Vogt, U. Alexiev, *Int. J. Mol. Sci.* **2015**, *16*, 6960; c) G. Zoubari, S. Staufenbiel, P. Volz, U. Alexiev, R. Bodmeier, *Eur. J. Pharm. Biopharm.* **2017**, *110*, 39.
[6] E. Parrish, M. A. Caporizzo, R. J. Composto, *J. Chem. Phys.* **2017**, *146*, 203318.
[7] a) Y. Li, J. Schnekenburger, M. Duits, *J. Biomed. Opt.* **2009**, *14*, 064005; b) H. Tada, H. Higuchi, T. M. Wanatabe, N. Ohuchi, *Cancer Res.* **2007**, *67*, 1138.
[8] K. A. Rose, M. Molaei, M. J. Boyle, D. Lee, J. C. Crocker, R. J. Composto, *J. Appl. Phys.* **2020**, *127*, 191101.
[9] N. Chenouard, I. Smal, F. de Chaumont, M. Maska, I. F. Sbalzarini, Y. H. Gong, J. Cardinale, C. Carthel, S. Coraluppi, M. Winter, A. R. Cohen, W. J. Godinez, K. Rohr, Y. Kalaidzidis, L. Liang, J. Duncan, H. Y. Shen, Y. K. Xu, K. E. G. Magnusson, J. Jalden, H. M. Blau, P. Paul-Gilloteaux, P. Roudot, C. Kervrann, F. Waharte, J. Y. Tinevez, S. L. Shorte, J. Willemse, K. Celler, et al., *Nat. Methods* **2014**, *11*, 281.
[10] K. Jaqaman, D. Loerke, M. Mettlen, H. Kuwata, S. Grinstein, S. L. Schmid, G. Danuser, *Nat. Methods* **2008**, *5*, 695.
[11] S. Manley, J. M. Gillette, G. H. Patterson, H. Shroff, H. F. Hess, E. Betzig, J. Lippincott-Schwartz, *Nat. Methods* **2008**, *5*, 155.
[12] S. Semrau, T. Schmidt, *Biophys. J.* **2007**, *92*, 613.
[13] M. J. Saxton, *Nat. Methods* **2008**, *5*, 671.
[14] C. M. Anderson, G. N. Georgiou, I. E. G. Morrison, G. V. W. Stevenson, R. J. Cherry, *J. Cell Sci.* **1992**, *101*, 415.
[15] I. Chauhan, M. Yasir, M. Verma, A. P. Singh, *Adv. Pharm. Bull.* **2020**, *10*, 150.
[16] U. Alexiev, D. L. Farrens, *Biochim. Biophys. Acta, Bioenerg.* **2014**, *1837*, 694.
[17] W. B. Asher, P. Geggier, M. D. Holsey, G. T. Gilmore, A. K. Pati, J. Meszaros, D. S. Terry, S. Mathiasen, M. J. Kaliszewski, M. D. McCauley, A. Govindaraju, Z. Zhou, K. G. Harikumar, K. Jaqaman, L. J. Miller, A. W. Smith, S. C. Blanchard, J. A. Javitch, *Nat. Methods* **2021**, *18*, 397.
[18] M. E. Sommer, K. P. Hofmann, M. Heck, *Nat. Commun.* **2012**, *3*, 995
[19] P. R. Robinson, G. B. Cohen, E. A. Zhukovsky, D. D. Oprian, *Neuron* **1992**, *9*, 719.
[20] R. Vogel, T. P. Sakmar, M. Sheves, F. Siebert, *Photochem. Photobiol.* **2007**, *83*, 286.
[21] T. Y. Kim, H. Uji-i, M. Moller, B. Muls, J. Hofkens, U. Alexiev, *Biochemistry* **2009**, *48*, 3801.
[22] M. Gunkel, J. Schoneberg, W. Alkhaldi, S. Irsen, F. Noe, U. B. Kaupp, A. Al-Amoudi, *Structure* **2015**, *23*, 628.
[23] V. Levi, Q. Ruan, K. Kis-Petikova, E. Gratton, *Biochem. Soc. Trans.* **2003**, *31*, 997.
[24] R. Parthasarathy, *Nat. Methods* **2012**, *9*, 724.
[25] a) F. Persson, M. Linden, C. Unoson, J. Elf, *Nat. Methods* **2013**, *10*, 265; b) R. Zhao, J. H. Yuan, N. Li, Y. H. Sun, T. Xia, X. H. Fang, *Anal. Chem.* **2019**, *91*, 13390; c) J. N. A. Vink, S. J. J. Brouns, J. Hohlbein, *Biophys. J.* **2020**, *119*, 1970.
[26] R. Barnkob, M. Rossi, *J. Open Res. Software* **2021**, *9*, 22.
[27] J. H. McDowell, H. Kuhn, *Biochemistry* **1977**, *16*, 4054.
[28] a) U. Wilden, H. Kuhn, *Biochemistry* **1982**, *21*, 3014; b) K. Kirchberg, T.-Y. Kim, M. Möller, D. Skegro, G. Dasara Raju, J. Granzin, G. Büldt, R. Schlesinger, U. Alexiev, *Proc. Natl. Acad. Sci. U. S. A.* **2011**, *108*, 18690.
[29] S. Bhattacharya, K. D. Ridge, B. E. Knox, H. G. Khorana, *J. Biol. Chem.* **1992**, *267*, 6763.
[30] S. J. Holden, S. Uphoff, A. N. Kapanidis, *Nat. Methods* **2011**, *8*, 279.
[31] H. Solomon, *Geometric Probability*, 1st ed., Society for Industrial and Applied Mathematics, Philadelphia **1978**.
[32] T. Kues, A. Dickmanns, R. Luhrmann, R. Peters, U. Kubitscheck, *Proc. Natl. Acad. Sci. U. S. A.* **2001**, *98*, 12021.
[33] M. J. Saxton, *Biophys. J.* **1993**, *64*, 1766.